



Promotion of Different Active Phases in $\text{MnO}_x\text{-CeO}_2$ Catalysts for Simultaneous NO Reduction and o-DCB Oxidation

J. A. Martín-Martín¹ · M. P. González-Marcos¹ · A. Aranzabal¹ · J. R. González-Velasco¹ · E. Finocchio²

Accepted: 5 July 2024
© The Author(s) 2024

Abstract

$\text{MnO}_x\text{-CeO}_2$ catalysts with different Mn and Ce content were prepared to evaluate the effect of metal content on catalytic properties and activity in the simultaneous NO reduction and o-DCB oxidation, in order to elucidate the most active species for the process. Catalytic properties were evaluated by ICP-AES, XRD, skeletal FTIR, STEM-HAADF, XPS, N_2 -physisorption, H_2 -TPR, NH_3 -TPD and pyridine-FTIR. Catalysts with 85%Mn and 15%Ce molar content have been found to be the most active. Their excellent catalytic performance is related to the coexistence of Mn in different phases, i.e., Mn species strongly interacting with Ce and segregated Mn species. The effect of the preparation methods has also been deeply investigated: Co-precipitation method (CP) leads to Mn segregation as Mn_2O_3 , whereas sol-gel preparation method (SG) promotes the formation of an amorphous powder. The synergy between segregated Mn_2O_3 species and Mn species in high interaction with Ce (resulting in a mixed oxide phase) leads to the presence of Mn with different oxidation states. This effect, together with the high oxygen mobility caused by structural defects, enhances redox, acidic and oxidative properties. The improvement of catalytic properties with Mn content also favors NO reduction side-reactions, with N_2O and NO_2 being the most important by-products, whereas it limits the production of chlorinated organic by-products in o-DCB oxidation.

Highlights

- High Mn content, 85%Mn-15%Ce (molar), leads to the best catalytic activity.
- At low Mn content, Mn incorporates into cerium oxide structure (mixed oxide phase).
- At high Mn content, Mn gradually segregates as manganese oxide.
- Co-precipitation enhances morphological properties compared to sol-gel synthesis.
- The synergy between Mn in high interaction with Ce and segregated Mn is key for catalytic activity.

Keywords Mn and Ce content · NO reduction · o-DCB oxidation · Segregated Mn · Mixed oxides

1 Introduction

Sustainable waste management is one of the most important challenges our society has to face in the short term. Current regulations on this issue establish a hierarchy in which any way of waste recovery is prioritized over landfilling [1]. Incineration of municipal solid waste is considered to be a suitable way of recovering the energy contained in waste and using it to produce heat and/or electricity. Thus, incineration with high level of energy recovery is considered as a waste to energy process [2, 3]. Nonetheless, there is a certain rejection in the society due to the fact the combustion stage of incineration processes produces a wide variety of pollutants, such as dust, heavy metals, acid gases, nitrogen

✉ M. P. González-Marcos
mp.gonzalezmarcos@ehu.eus

¹ Department of Chemical Engineering, Faculty of Science and Technology, Group of Chemical Technologies for Environmental Sustainability, The University of the Basque Country, UPV/EHU, P.O. Box 644, Bilbao E-48080, Spain

² Dipartimento di Ingegneria Civile, Chimica e Ambientale, Università di Genova, Via Opera Pia 15, Genova I-16145, Italy

oxides (NO_x), chlorinated compounds, etc., which must be abated to meet the emission limits.

In the latest years, the research on integration of NO_x and dioxins and furans (PCDD/Fs) removal has attracted extensive attention. NO_x are removed by selective reduction, through either a non-catalytic or a catalytic process. Selective catalytic reduction (SCR) allows to reach higher efficiency levels in terms of conversion, selectivity and reducing agent saving [4, 5]. Consequently, it is the best-positioned technology in view of the foreseeable tightening of emission limits for the future. On the other hand, PCDD/Fs are mostly abated by adsorption, which allows to meet the emission limits, but it has the disadvantage of not destroying the pollutants and generating a waste that needs further treatment [6, 7].

The traditional catalyst for SCR units, based on vanadium oxide [4], is reported to be also active to carry out the catalytic oxidation of PCDD/Fs [8, 9]. This catalyst offers the possibility of removing two different pollutants in a single stage. Hence, the advantages of SCR on the removal of NO_x will be added to those of catalytic oxidation, which would allow to destroy the PCDD/Fs through total oxidation. In fact, the simultaneous removal of both pollutants is already reported on the Best Available Techniques reference document for waste incineration by the JRC [10].

Currently, SCR units are located at the end of the gas cleaning line to avoid the poisoning of the catalyst by some pollutants, such as SO_2 [11]. Because of this, the temperature of the gas feeding stream is below the operating temperature of the SCR unit, so that it must be heated, which consumes energy resources [12]. For this reason, commercial SCR systems demand to operate at lower temperature in order to avoid heating costs. This inevitably means the use of more active catalytic formulations to perform SCR at lower temperatures.

In this sense, transition metal oxide catalysts have been widely studied in recent years for low temperature SCR [13–15]. Among them, Mn-based catalysts are the most reported ones because of the variability in oxidation states and crystal phases, which offers the possibility of having a wide variety of active species. MnO_2 is considered as the most active manganese oxide in SCR [16, 17]. Tang and co-workers [18] evidenced a higher catalytic activity of amorphous manganese oxide in comparison to crystalline manganese oxide in the low temperature SCR. Moreover, Kang and co-workers [19] studied the effect of calcination temperature and precipitating agent. Catalytic activity of Mn-based catalysts can be notably enhanced by doping with other transition metal, such as Cu, Co, Fe, Ce, etc. [20–23]. Among them, Ce doping is the most widely studied, as it favors the promotion of oxygen vacancies and also allows Mn incorporation to the CeO_2 structure leading to a mixed

oxide phase. Qi and co-workers [24] studied $\text{MnO}_x\text{-CeO}_2$ catalysts prepared by co-precipitation and reported NO conversion around 95% at 150 °C. In the same way, Shen and co-workers [25] obtained NO conversion above 90% with $\text{MnO}_x/\text{CeO}_2$ supported catalysts. The positive effect of Mn content on NO conversion has been also highlighted by Liu and co-workers [26], although it causes at the same time a decrease in N_2 selectivity.

$\text{MnO}_x\text{-CeO}_2$ catalytic formulation is also reported in the literature to be active in oxidation reactions of organic compounds, such as toluene, ethanol, acetaldehyde [27, 28] and chlorinated organic compounds, such as chlorinated benzenes and trichloroethylene [29, 30]. In this sense, Wu and co-workers [31] reported total conversion of o-xylene above 250 °C with $\text{MnO}_x\text{-CeO}_2$ catalysts. Similarly, Xingyi and co-workers [32] concluded that the increase in Mn content favors chlorobenzene conversion. The fact that $\text{MnO}_x\text{-CeO}_2$ catalytic formulation is active for oxidation reactions suggests that this formulation can be also active on the oxidation of PCDD/Fs, making the simultaneous removal of NO_x and PCDD/Fs feasible.

It is well known that preparation method plays a key role on the interaction degree between Mn and Ce in $\text{MnO}_x\text{-CeO}_2$ catalysts [33, 34]. Previous research has shown that co-precipitation and sol-gel favor a high interaction between Mn and Ce, which means Mn incorporates into CeO_2 structure leading to a mixed oxide phase, and oxygen vacancies are promoted [35]. Those facts allow the formation not only of Mn and Ce highly active species, but also of active oxygen species to perform the reactions. In addition to the interaction degree, metal content also plays an important role on the active species present in the catalysts, as it can change the crystallinity of the sample and the ratio Ce/Mn.

This work aims to assess the effect of Mn and Ce content on $\text{MnO}_x\text{-CeO}_2$ catalysts prepared by two methods that ensure a high interaction degree between these metals, in order to find which active species is the most active in NO reduction carried out simultaneously with the oxidation of o-DCB (this one used as model compound of PCDD/Fs).

2 Experimental

2.1 Catalyst Preparation

In order to assess the Mn and Ce content and to elucidate which active species favors catalytic activity, three bimetallic samples with different compositions have been studied: one rich in Ce (15%mol Mn and 85%mol Ce, named 15Mn85Ce), a second one with equimolar composition (50%mol Mn and 50%mol Ce, named 50Mn50Ce) and the third one rich in Mn (85%mol Mn and 15%mol Ce, named

85Mn15Ce). For the synthesis of these samples, both coprecipitation (CP) and sol-gel (SG) methods were used, since our previous research has proven they provide a high interaction between Mn and Ce [35].

The procedure followed in each preparation method is explained in the following.

2.1.1 Co-precipitation

The proper amount of precursor compounds, $\text{Mn}(\text{NO}_3)_2 \cdot 4\text{H}_2\text{O}$ and $\text{Ce}(\text{NO}_3)_3 \cdot 6\text{H}_2\text{O}$, was solved in distilled water at room temperature. Subsequently, a 1.3 M solution of ammonium carbamate ($\text{H}_2\text{NCOONH}_4$) was added drop by drop until reaching a pH value of 9 to precipitate the metal cations. The resulting suspension was aged for 2 h and, then, filtered and washed with distilled water. The obtained solid was dried for 12 h at 110 °C and calcined in static air at 500 °C for 3 h with a heating ramp of 1 °C/min. Finally, the catalyst was sieved to 0.3–0.5 mm to avoid mass transfer limitations in the catalytic tests. Three bimetallic catalysts were prepared with a molar composition of 15%Mn and 85%Ce (15Mn85Ce CP), 50%Mn and 50%Ce (50Mn50Ce CP) and 85%Mn and 15%Ce (85Mn15Ce CP). Pure cerium oxide (CeO_2 CP) and manganese oxide (MnO_x CP) were also prepared following this procedure.

2.1.2 Sol-gel

The proper amount of precursor compounds, $\text{Mn}(\text{NO}_3)_2 \cdot 4\text{H}_2\text{O}$ and $\text{Ce}(\text{NO}_3)_3 \cdot 6\text{H}_2\text{O}$, was solved in distilled water at room temperature. As chelating agent, citric acid was also added to the solution with a molar ratio of 0.3(Mn+Ce). Subsequently, the temperature of this solution was progressively increased to 80 °C in continuous stirring leading to the evaporation of the solvent and the formation of the gel. The obtained gel was dried for 12 h at 110 °C and calcined in static air at 500 °C for 3 h with a heating ramp of 1 °C/min. Finally, the catalyst was sieved to 0.3–0.5 mm to avoid mass transfer limitations. Three bimetallic catalysts were prepared with a molar composition of 15%Mn and 85%Ce (15Mn85Ce SG), 50%Mn and 50%Ce (50Mn50Ce SG) and 85%Mn and 15%Ce (85Mn15Ce SG). Pure cerium oxide (CeO_2 SG) and manganese oxide (MnO_x SG) were also prepared following this procedure.

2.2 Catalyst Characterization

Actual metallic content was analyzed by inductively coupled plasma atomic emission spectroscopy (ICP-AES). The samples were dissolved in HCl: HNO_3 (3:1 molar ratio), and the measurements carried out in a Horiba Yobin Activa equipment.

X-ray diffraction (XRD) was used to identify the different crystal phases composing the samples and their crystallinity degree. The analysis was performed on a Philips PW 1710 X-ray diffractometer with Cu $K\alpha$ radiation ($\lambda = 1.5406$ Å) and Ni filter. The measurements were ranged between 20 and 60° (2 θ) with step size of 0.026° and counting time of 528 s. The crystal phases composing the samples were identified by comparing with JCPDS database cards.

Skeletal FTIR was also used to analyze structural properties of the samples. The analysis was carried out in Nicolet 380 and Thermo Nicolet Nexus Fourier Transform instruments in the range of 4000–400 cm^{-1} (100 scans with a resolution of 4 cm^{-1}). For the analysis, all samples were diluted in KBr and pressed in discs of 0.7 g approximately.

STEM-HAADF images with elemental maps were carried out in a FEI Titan Cubed G2 60–300 electron microscope working at 200 kV and equipped with a Super-X EDX system, high-brightness X-FEG Schottky field emission electron gun, monochromator and CEOS GmbH spherical aberration corrector (Cs). These components operate under a HAADF detector in STEM mode (camera of 180 mm). Prior to the analysis, the samples were dispersed in ethanol using an ultrasonic bath.

XPS measurements were performed in a SPECS spectrometer with a Phoibos 150 1D-DLD analyzer and a monochromatic radiation source Al $K\alpha$ (1486.7 eV). The sample pelletized in a disc was degassed and introduced in an ultra-high vacuum chamber (10^{-6} Pa). Firstly, the elements present in the sample were identified (0.1 s, 80 eV), and then the detailed analysis of the identified elements was carried out (0.1 s, 30 eV) with an exit angle of 90°. All spectra were referenced to C 1s. The results were analyzed with CASA XPS software, involving Shirley background subtraction and deconvolution of the spectra using mixed Gaussian-Lorentzian function.

Textural properties of the samples were evaluated by N_2 adsorption-desorption. The analysis was performed on a Micromeritics TRISTAR II 3020 at –196 °C. Prior to the analysis, the samples were pre-treated with a flow of N_2 at 350 °C for 4 h. BET procedure was used to calculate the specific surface area by using the data obtained from the adsorption isotherm branch in the relative pressure between 0.03 and 0.3. Average pore size was estimated according to BJH method using the resulting data from the desorption isotherm branch.

Redox properties of the samples were evaluated by temperature programmed reduction with H_2 (H_2 -TPR) on a Micromeritics AutoChem 2920 instrument. Firstly, for the pretreatment of the samples, each one (15–20 mg) was exposed to 50 cm^3/min of 5% O_2/He mixture at 500 °C for 45 min and, then, the temperature was decreased to 100 °C in helium. After pretreatment, the samples were exposed to 50

cm³/min of 5% H₂/Ar while the temperature increased from 100 to 900 °C at 10 °C/min. A TCD was used to record the H₂ consumption in the experiments. In order to avoid interferences between the water produced and the TCD measurement, water was trapped in a cold trap. H₂ consumed in the experiments was calculated by time-integration of TCD signal. The signals were deconvoluted to Gaussian-type peaks.

Temperature programmed desorption of ammonia (NH₃-TPD) was carried out to study the acidity of the samples and the strength of acid sites. The analysis was performed on a Micromeritics AutoChem 2920 instrument. As a pretreatment, each sample (15–20 mg) was treated in 50 cm³/min of 5% O₂/He mixture at 500 °C for 45 min and then the temperature was decreased to 50 °C in helium. After pretreatment, the adsorption of ammonia was carried out by exposing the samples to 130 cm³/min of 1% NH₃/He gas mixture at 50 °C for 60 min. Ammonia weakly adsorbed was removed by feeding 130 cm³/min of He for 60 min at the same temperature than the adsorption step. Finally, the ammonia strongly adsorbed on the catalytic surface was desorbed by heating the sample from 50 to 500 °C with a heating ramp of 10 °C/min and using helium as a carrier. A TCD was used to measure the NH₃ desorbed. Total acidity was calculated by time-integration of TCD signal. The signals were deconvoluted to Gaussian-type peaks.

FTIR spectra of adsorbed pyridine was used to study the nature of the acid sites. The experiments were carried out on a ThermoNicolet Nexus FT instrument. Before the analysis, pure powder samples were pressed into a self-supporting disc and pretreated at 480 °C in static air for 30 min and then in vacuum (1.3·10⁻¹ Pa) for 30 min, in order to avoid the reduction of the catalyst surface. Subsequently, pyridine adsorption was carried out at a pressure of 263.4 Pa at room temperature. The spectra of the adsorbed species were recorded after outgassing.

2.3 Reaction Set-up and Catalytic Tests

The reaction set-up generates a gas feeding stream similar in components and concentrations to the stream found at the inlet of a SCR unit with tail-end configuration of an incineration plant. The feeding of each reagent, either gas or liquid, is controlled by mass flow controllers (Bronkhorst[®] High-Tech F-201CV, for gases, and Bronkhorst[®] High-Tech μ-Flow L01-AAA-99-0-20 S, for liquids). To ensure complete evaporation and homogeneous mixture of liquid and gaseous components, the reaction set-up has a controlled-evaporator-mixer (Bronkhorst[®] High-Tech W-102 A-111-K) and electrical resistances for heating all pipes.

The feeding stream for catalytic activity test is composed by NO (300 ppm), NH₃ (300 ppm), O₂ (10%), o-DCB (100 ppm) and Ar to balance. o-DCB was used in oxidation

reaction instead of PCDD/Fs because PCDD/Fs have a high toxicity and working with them at lab scale involves operational problems. The catalytic bed is composed of 1.5 g of sieved catalyst (particle size between 0.3 and 0.5 mm) and inert quartz sieved between 0.5 and 0.8 mm, resulting in a final volume of 3 cm⁻¹. The catalytic activity was assessed by light-off experiments with a feeding stream of 2 L_N/min (GHSV 40,000 h⁻¹) at a pressure of 1520 kPa while reaction temperature increased from 100 to 450 °C with a constant heating rate of 1.5 °C/min. Before each experiment, as a pretreatment, the catalytic bed was exposed to 2 L_N/min of pure Ar at 200 °C for 2 h.

Several analyzers were used to measure the concentration of reaction reagents and products: an ABB Limas 21 for the measurement of NO, NO₂ and NH₃, an ABB Uras 26 Infrared analyzer for the measurement of N₂O, CO and CO₂, and a gas chromatograph (Agilent Technologies 7890 A) with a mass selective detector (Agilent Technologies 5975 C) to measure the o-DCB concentration and the chlorinated organic compounds formed in o-DCB oxidation. Here, it is important to note that NH₃ concentration could not be measured because of o-DCB interference on ABB Limas 21.

NO and o-DCB conversion were calculated from Eqs. (1) and (2), respectively. Selectivity to CO₂ and CO was calculated through Eqs. (3) and (4), respectively.

$$X_{\text{NO}} = \frac{C_{\text{NO},in} - C_{\text{NO},out}}{C_{\text{NO},in}} \cdot 100 \quad (1)$$

$$X_{\text{o-DCB}} = \frac{C_{\text{o-DCB},in} - C_{\text{o-DCB},out}}{C_{\text{o-DCB},in}} \cdot 100 \quad (2)$$

$$S_{\text{CO}_2} = \frac{C_{\text{CO}_2,out}}{6 \cdot C_{\text{o-DCB},in} - C_{\text{o-DCB},out}} \cdot 100 \quad (3)$$

$$S_{\text{CO}} = \frac{C_{\text{CO},out}}{6 \cdot (C_{\text{o-DCB},in} - C_{\text{o-DCB},out})} \cdot 100 \quad (4)$$

3 Results and Discussion

3.1 Catalytic Characterization

Table 1 includes actual metallic contents of the bulk catalysts, as determined by ICP-AES measurements, as well as the Mn/Ce molar ratio. The obtained compositions are in good agreement with the nominal contents.

XRD has been firstly used to evaluate the effect of Mn and Ce content on structural properties. Figure 1 shows the diffraction patterns of composite oxides prepared by sol-gel and co-precipitation with different content of active

Table 1 Actual metallic content and bulk Mn/Ce molar ratio of MnO_x-CeO₂ samples prepared by sol-gel and co-precipitation, derived from ICP-AES

Sample	Sol-gel			Co-precipitation		
	Mn (mol%)	Ce (mol%)	Mn/Ce	Mn (mol%)	Ce (mol%)	Mn/Ce
CeO ₂	0.0	100.0	0	0.0	100.0	0
15Mn85Ce	15.0	85.0	0.18	11.8	88.2	0.13
50Mn50Ce	49.4	50.6	0.98	48.1	51.9	0.93
85Mn15Ce	83.6	16.4	5.10	84.6	15.4	5.49
MnO _x	100.0	0.0	--	100.0	0.0	--

metals, together with the diffraction patterns of pure cerium and manganese oxide. Pure cerium oxide exhibits diffraction peaks characteristic of fluorite crystal phase, typical of CeO₂, whereas diffraction peaks of pure manganese oxide correspond to α -Mn₂O₃ crystal phase. Only one curve is shown in Fig. 1 for cerium oxide and manganese oxide because no significant difference has been found with preparation procedure in the XRD patterns of pure oxides.

As for bimetallic samples, irrespectively of the preparation method, those with the lowest Mn content (15Mn85Ce) only show diffraction peaks related to fluorite phase, although they are broader than those observed for pure cerium oxide. Moreover, the position of these peaks is shifted to higher Bragg angles, especially in those samples prepared by sol-gel. On the other hand, in the samples with the highest Mn content (85Mn15Ce), different results are clearly observed depending on the preparation method. Thus, sol-gel leads to a mostly amorphous solid with weak diffraction peaks at 28.8 and 37.4° associated to MnO₂, whereas co-precipitation promotes the co-existence of two different phases, which are clearly evidenced by the diffraction peaks of Mn₂O₃ crystal phase at 33.3 and 35.5° together with those already present at lower Mn contents of fluorite phase.

The broadening of fluorite peaks and their shift towards higher Bragg angles in samples with different Mn and Ce contents suggests the incorporation of Mn to fluorite structure of CeO₂ forming mixed oxide phase or solid solution phase [36]. This incorporation is thought to be total in 15Mn85Ce and 50Mn50Ce samples, as their diffraction patterns show no diffraction peaks of manganese oxide. Mixed oxide phase favors the formation of Mn species strongly interacting with Ce, which should cause a distortion of fluorite phase. In order to evaluate this distortion and corroborate the formation of a mixed oxide phase, the lattice parameter of fluorite phase has been estimated and it is summarized in Table 2.

In the catalysts prepared by sol-gel, increasing Mn content leads to a significant decrease in the fluorite lattice parameter, except in the sample with the highest Mn content, where fluorite phase disappears. The decrease in lattice parameter is associated to the contraction of fluorite structure as a consequence of the smaller ionic radius of Mn ions

with respect to Ce ions [29]. Thus, these results corroborate the formation of mixed oxide phase and evidence that the contribution of Mn species interacting with Ce increases with Mn content.

Similarly, increasing Mn content in the catalysts prepared by co-precipitation leads to a decrease in the lattice parameter. However, the sample with the highest Mn content (85Mn15Ce CP) has a higher value of lattice parameter than the 50Mn50Ce CP sample, but lower than pure cerium oxide. This result denotes the presence of mixed oxide also in the 85Mn15Ce CP sample, although its contribution is lower than in catalysts with lower Mn contents. This effect is associated to such high Mn content causing a saturation of fluorite phase, which leads to Mn segregation producing segregated Mn₂O₃ species, as revealed by the appearance of Mn₂O₃ peaks in the diffraction pattern of 85Mn15Ce CP sample. A similar saturation of fluorite phase was observed by Ye and Xu [37], who concluded that the maximum Mn content being able to enter fluorite structure is limited to a 0.7 molar ratio.

On the other hand, Table 2 also summarizes the crystal size of fluorite phase, which was estimated according to Scherrer equation. The increase in Mn content clearly produces a decrease in fluorite crystal size. This result agrees with the trend in lattice parameter just discussed, and it is associated to Mn incorporation into fluorite generating structural defects, which has a negative effect on the growth of fluorite crystal domains. The presence of structural defects plays a fundamental role in the formation of oxygen vacancies, which favor high mobility and storage capacity of oxygen throughout catalytic structure.

In order to obtain more structural information, skeletal FTIR analysis has been performed. Figure 2a and b show the spectra of samples with different Mn and Ce contents prepared by sol-gel and co-precipitation, respectively.

Pure cerium oxides exhibit two broad bands around 700 and 500 cm⁻¹ characterizing the fluorite structure, the latter being related to the longitudinal optical mode of fluorite, whose transverse mode is reported to be located at 360 cm⁻¹ [38]. The weak bands at 1060 and 850 cm⁻¹ are associated to vibrations of Ce-O bonds [39, 40]. Moreover, other bands at higher wavenumber denote the presence of surface adsorbed species. For instance, the band at 1625 cm⁻¹ is

Table 2 Structural properties of $\text{MnO}_x\text{-CeO}_2$ samples with different Mn and Ce content prepared by sol-gel and co-precipitation

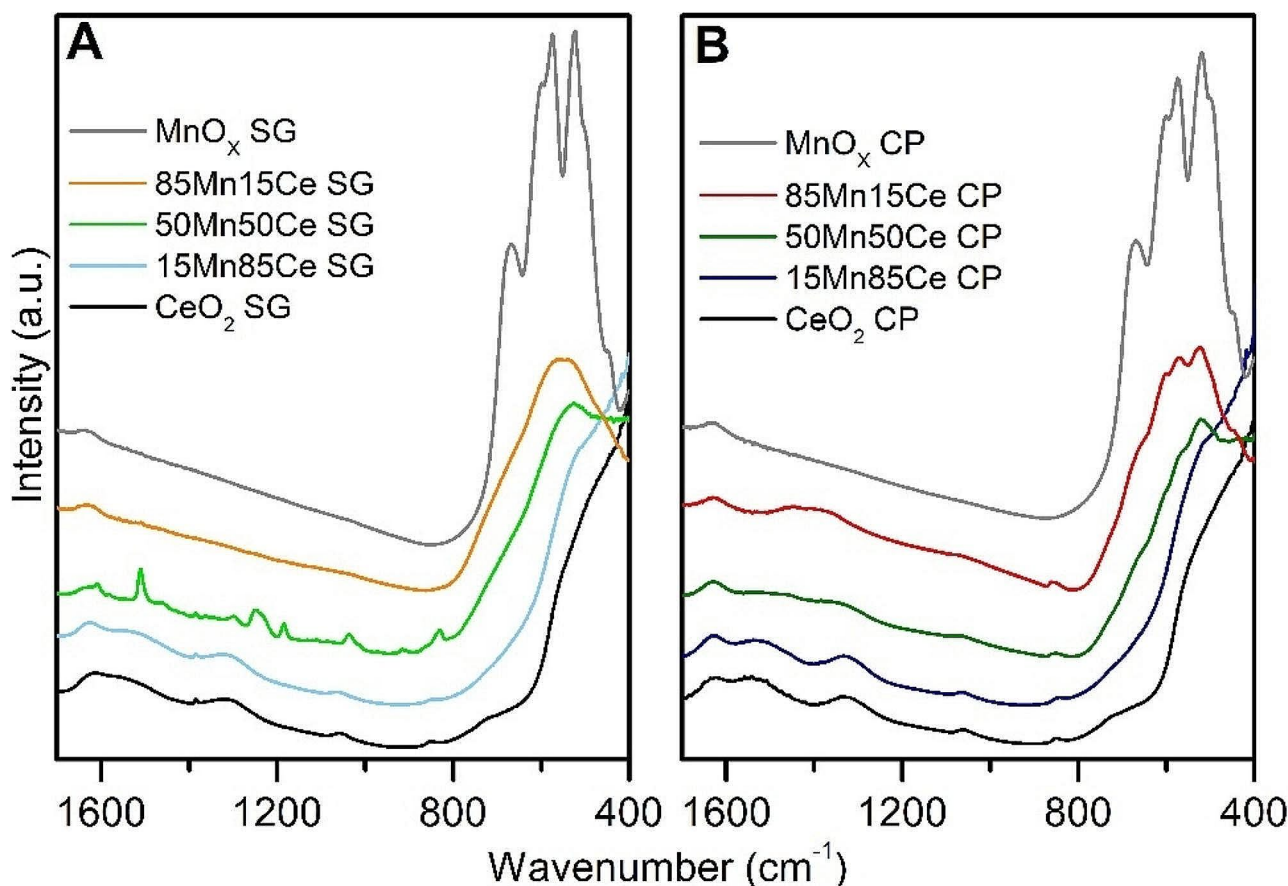
Sample	Fluorite lattice parameter (nm)		Fluorite crystal size (nm)	
	Sol-gel	Co-precipitation	Sol-gel	Co-precipitation
CeO_2	5.4179	5.4135	9	9
15Mn85Ce	5.4027	5.4054	4	5
50Mn50Ce	5.3855	5.4035	3	4
85Mn15Ce	--	5.4107	--	4
MnO_x	--	--	--	--

mainly related to vibration modes of molecularly adsorbed water [39] and the weak bands around 1538 and 1327 cm^{-1} are associated to surface carbonates. Pure manganese oxides CP and SG show similar spectra with bands at 670 , 600 , 570 , 500 , 525 and 450 cm^{-1} , which are typically related to vibrational modes of $\alpha\text{-Mn}_2\text{O}_3$ [41].

In bimetallic samples, the increase in Mn content leads to a growth of the shoulder located at 550 cm^{-1} . At lower wavenumber, the slope of the absorbance profile decreases, reaching a plateau in the 50Mn50Ce sample. This effect can be due to the appearance of another contribution in this

wavenumber range related to the increase in Mn content and the simultaneous decrease in Ce content, which produces a decrease in Ce-O bonds and the modification of the original structure of pure cerium oxide, as a consequence of Mn incorporation. In agreement with XRD data, this result supports the formation of a mixed oxide. In fact, the decreasing of fluorite bands with the increase in Mn content produces an isosbestic point around $450\text{--}435\text{ cm}^{-1}$, also reported by Escribano and co-workers [38] in Ce-Zr composite oxides.

The increase in Mn content to 85% leads to the appearance of manganese oxide bands in the range of $800\text{--}500\text{ cm}^{-1}$, although these bands have a higher definition degree in the sample prepared by co-precipitation, which supports what was previously concluded by XRD, i.e., co-precipitation method favors a higher crystallinity than sol-gel. On the other hand, despite the high crystallinity of manganese oxide phase in the 85Mn15Ce CP catalyst, some differences are observed in comparison to pure manganese oxide, especially in the $700\text{--}450\text{ cm}^{-1}$ region, where, for example, the band located at 670 cm^{-1} is not as well defined as in the pure manganese oxide. This fact can be associated to the modification of vibrational modes of manganese

**Fig. 2** Skeletal FTIR spectra of $\text{MnO}_x\text{-CeO}_2$ catalysts with different Mn and Ce content prepared by (a) sol-gel and (b) co-precipitation

oxide as a consequence of the strong interaction of Mn with Ce ions. Thus, this result supports those obtained by XRD for 85Mn15Ce CP sample, where a coexistence of fluorite substituted with Mn and segregated Mn_2O_3 was evidenced.

To get an in-depth view of the elemental composition at the catalytic surface, the bimetallic samples with the lowest and highest Mn content, 15Mn85Ce and 85Mn15Ce, were

evaluated by transmission electron microscopy high-angle annular dark field (STEM-HAADF) coupled to EDX. Figure 3 shows the HAADF images and the resulting elemental maps for Mn (red) and Ce (green). The EDX spectrum of selected surface regions of each sample are also provided. The 15Mn85Ce catalysts prepared by sol-gel and coprecipitation are characterized by a homogeneous distribution of

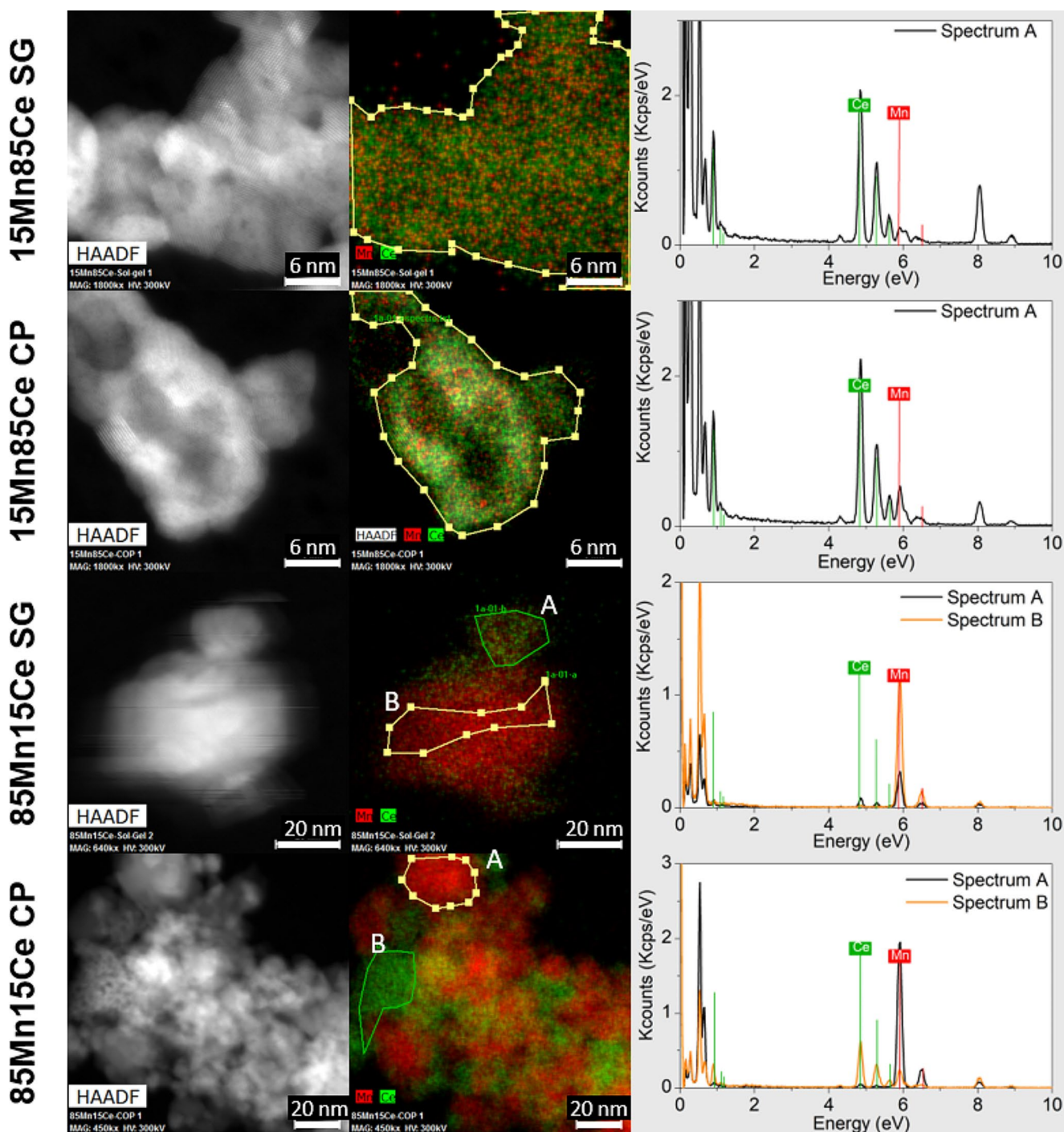


Fig. 3 STEM-HAADF images and EDX maps of selected $\text{MnO}_x\text{-CeO}_2$ samples. Mn in red and Ce in green. SG, catalysts prepared by sol-gel; CP, catalysts prepared by co-precipitation

Table 3 XPS results of MnO_x-CeO₂ samples with different Mn and Ce content prepared by sol-gel and co-precipitation

Samples	Sol-gel			Co-precipitation		
	Mn oxidation state ^a	Ce ³⁺ /Ce ⁴⁺ ^a	Mn/Ce ^a	Mn oxidation state ^a	Ce ³⁺ /Ce ⁴⁺ ^a	Mn/Ce ^a
CeO ₂	--	0.35	0	--	0.32	0
15Mn85Ce	3.47	0.23	0.16	3.47	0.17	0.11
50Mn50Ce	3.54	0.22	0.57	3.48	0.18	0.26
85Mn15Ce	3.56	0.20	3.78	3.47	0.16	2.55
MnO _x	3.51	--	--	3.48	--	--

^a Average values at the surface

Table 4 Textural properties of MnO_x-CeO₂ samples with different Mn and Ce content prepared by sol-gel and co-precipitation

Sample	Sol-gel			Co-precipitation		
	S _{BET} (m ² /g)	V _{pore} (cm ³ /g)	D _{pore} (nm)	S _{BET} (m ² /g)	V _{pore} (cm ³ /g)	D _{pore} (nm)
CeO ₂	60	0.11	6.2	80	0.12	6.3
15Mn85Ce	67	0.14	7.2	84	0.18	7.8
50Mn50Ce	63	0.16	8.5	88	0.21	8.0
85Mn15Ce	57	0.15	8.0	87	0.25	9.0
MnO _x	15	0.10	23.8	34	0.17	16.6

Mn and Ce, as pointed out by EDX spectra, although the peaks associated to Mn are much less intense than those of Ce, in agreement with the low Mn content. The good dispersion of Mn along the catalytic structure is in accordance with the results obtained from the structural analysis, in which the presence of Mn species interacting with Ce was evidenced as a consequence of the promotion of mixed oxide phase.

On the other hand, a phase segregation is clearly observed in the 85Mn15Ce catalysts. In the case of the sample prepared by sol-gel, there are two different areas in the elemental map: one (Area A) in which Mn and Ce coexist with high interaction degree and another one (Area B) only composed by Mn. The spectrum of Area A indicates the presence of both metals, although unlike 15Mn85Ce catalysts, Mn is the major metal component. In Area B, the only presence of Mn is corroborated by the spectrum, which confirms the segregation of Mn. Interestingly, XRD results showed that segregated manganese oxide phase of the 85Mn15Ce SG catalyst has hardly any crystallinity, so this segregated phase should have an amorphous structure.

In the case of the 85Mn15Ce CP sample, the elemental map clearly shows there are several regions with different interaction degree between Mn and Ce. The spectrum of Area A evidences the presence of only Mn due to the segregation of this metal, whereas spectrum B corroborates the presence of both metals, although the contribution of Ce becomes more important than that of Mn. Interestingly, an additional view out of the regions marked in the map (there are no spectra of this regions) reveals the presence of other regions with strong interaction between active metals, but in which the contribution of Mn becomes more important than that of Ce. Thus, this result reveals the presence of a wide variety of regions with different interaction degree between

the active metals in the same particle of catalyst, which has not been observed in the same sample prepared by sol-gel.

Catalysis being a surface process, XPS measurements were carried out to obtain information on the chemical composition and oxidation states at the surface of the prepared MnO_x-CeO₂ catalysts. The results have been summarized in Table 3. According to the results, the oxidation state of Mn at the surface of all the Mn-containing samples remains similar regardless the preparation procedure (only slightly higher in sol-gel samples) in all the range of compositions, with an approximate equal proportion of Mn⁴⁺ and Mn³⁺ at the surface. Concerning Ce, the results in Table 3 show that there is a higher proportion of Ce⁴⁺ than Ce³⁺ at the surface of all the samples, slightly higher in co-precipitation than sol-gel samples to equal compositions, and higher in the mixed oxides compared to the pure CeO₂.

Table 3 also shows the molar ratio between Mn and Ce at the surface of the samples. As expected, Mn/Ce increases with the Mn content in the samples. Comparing these results with those in Table 1, derived from ICP-AES measurements, it becomes evident that the catalytic surface of the catalysts is enriched in cerium.

N₂ physisorption was used to evaluate the influence of Mn and Ce contents on morphological properties. It is important to note that all samples exhibit type IV isotherms according to IUPAC classification, so they belong to the group of mesoporous materials. Table 4 summarizes the values of specific surface area, mean pore volume and mean pore diameter.

In general, bimetallic samples have higher surface area and pore volume than pure manganese and cerium oxides. This result is explained by the presence of structural defects resulting from Mn and Ce interaction that promote an improvement of morphological properties. Comparing the

results obtained with each preparation method, co-precipitation leads to higher surface area and pore volume. The promotion of morphological properties in catalysts prepared by co-precipitation compared to other preparation methods, including sol-gel, was also reported by Martín-Martín and co-workers [35] and will have indeed an important role in the improvement of catalytic activity.

Interestingly, mean pore volume and mean pore diameter follow a similar trend up to the samples with equimolar composition (50Mn50Ce). Thus, the larger the Mn content, the higher the mean pore volume and size. However, different results are obtained for the 85Mn15Ce catalysts depending on the preparation method: in the co-precipitation series, the pore volume and size increase with respect to 50Mn50Ce, whereas in the catalyst prepared by sol-gel both parameters decrease. This different trend is to be related to the different structural properties that each preparation method favors at such Mn content.

The effect of Mn and Ce content on redox properties was studied by H₂-TPR. Figure 4a and b show the reduction profiles of the samples prepared by sol-gel and co-precipitation, respectively. The reduction profiles of pure cerium oxides (prepared by both CP and SG) exhibit two wide reduction peaks, one around 500 °C, related to surface Ce reduction,

and another one around 800 °C, corresponding to the reduction of bulk Ce [26], the one prepared by co-precipitation shifted around 50 °C to lower temperature. Deconvolution of the profiles (see Fig. 4) requires several Gaussian peaks to adequately fit the low temperature reduction peak, what indicates that several reduction processes, associated to different surface environments and/or crystal sizes, are taking place simultaneously.

In the same way, the reduction profiles of pure CP and SG manganese oxides are quite similar; composed by two peaks around 330 and 470 °C, which fit very well with the reduction of Mn₂O₃ [17, 42], in agreement with the results of XRD. Again, the reduction profile for the CP sample is significantly shifted to lower temperatures (around 100 °C), and the peaks are sharper. The peak located at lower temperature is associated to the reduction of Mn₂O₃ to Mn₃O₄; and the other one to the reduction of Mn₃O₄ to MnO. Although the profiles seem simple enough, deconvolution requires of at least six Gaussian peaks for an adequate description, which indicates that there is a wide variation of crystallinity within the samples. The reduction temperature of manganese oxides is known to be a function of crystallinity, so that different oxide phases cannot be distinguished just by their reduction temperature [41].

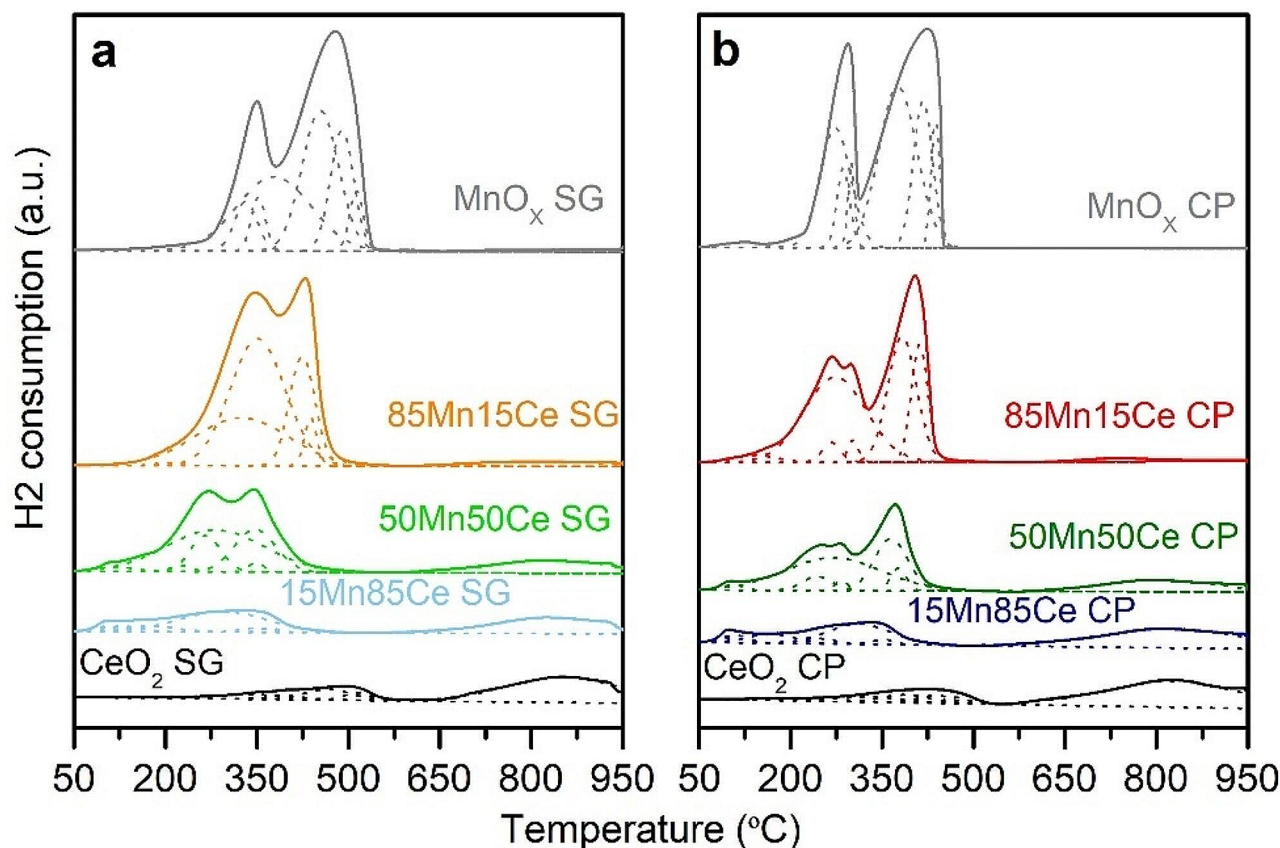


Fig. 4 H₂-TPR profiles of MnO_x-CeO₂ samples with different Mn and Ce content prepared by (a) sol-gel and (b) co-precipitation

The bimetallic CP and SG samples with the lowest Mn content have a reduction profile similar to that of pure cerium oxide (due to its low Mn content), although shifted towards lower temperatures. This effect suggests an improvement of redox properties likely due to the oxygen vacancies generated by structural defects caused by the Mn and Ce interaction. Moreover, the reduction profile of these samples has a tiny peak around 100 °C, related to the reduction of Mn highly dispersed on the surface [43], and another broad one around 275 °C, associated to the reduction of Mn embedded into CeO₂ lattice [32]. No clear effect of the preparation method can be evidenced here, which agrees with the results of STEM-HAADF-EDX.

The increase in Mn content leads to the appearance of at least two strong reduction peaks between 200 and 500 °C, mainly related to Mn reduction, being the contribution of surface Ce reduction by far smaller. Moreover, the reduction pattern of 50Mn50Ce CP and 85Mn15Ce CP samples show at least three components in this range. At higher temperatures, the H₂ uptake associated to some reduction of bulk Ce is also present, as evidenced by the broad signal around 800 °C. As in the samples with the lowest Mn content, the temperature at which Mn reduction occurs in the remaining bimetallic samples (both CP and SG) is lower than in pure manganese oxide due to the improvement of redox properties provided by Mn and Ce interaction. Whereas the temperature range for Mn reduction is similar in 50Mn50Ce SG and CP samples, reduction of 85Mn15Ce CP is shifted nearly 100 °C to lower temperatures compared to 85Mn15Ce SG.

Thus, the enhancement of redox properties provided by the interaction of Mn and Ce is not only evidenced by the shift of reduction peaks to lower temperatures, but also by their shapes. In fact, the Mn reduction peaks in bimetallic catalysts exhibit an increased complexity with peaks overlapping not observed in the reduction profile of pure manganese oxide. The strong overlap suggests the presence of different Mn species, which are being reduced at a similar temperature as a consequence of the high oxygen mobility and small particle size, as discussed in the following paragraphs.

In Table 5, the average bulk oxidation states of Mn species are reported, as estimated from the H₂ consumptions. Some assumptions have been considered for such estimations: (i) the H₂ consumption of Ce at low temperature is negligible (which means that the average Mn oxidation states given in Table 5 will be slightly overestimated, in particular for the Ce-rich samples), (ii) MnO is the final state of Mn reduction. From these results, the oxidation state of Mn in the samples prepared by sol-gel is close to Mn⁴⁺, so sol-gel method clearly favors this Mn species. On the contrary, the oxidation state of Mn in the samples prepared by co-precipitation decreases from Mn⁴⁺ to Mn³⁺ at increasing Mn content. This effect denotes that Mn segregation affects the oxidation state of Mn and, consequently, Mn species. In this way, Mn⁴⁺ is promoted at low Mn contents, where Mn is strongly interacting with Ce; whereas the increase in Mn content leads to a progressive Mn segregation that favors Mn³⁺ species, because of the formation of a segregated Mn₂O₃ phase in the samples prepared by co-precipitation, which was previously evidenced by means of structural analysis.

Average bulk Mn oxidation states in Table 5 can be compared with surface Mn oxidation states in Table 3. As commented above, the average oxidation state of Mn on the surface seems to be independent of the preparation procedure and Mn content, with about equal proportion of Mn⁴⁺ and Mn³⁺ at the surface. According to Table 5, surface average oxidation state of Mn is also independent of the average oxidation state of Mn in the bulk of the sample.

Although attempts to effectively assign peaks to specific species by deconvolution has been carried out, it was not possible, due to the high number of peaks and their complex evolution (see Fig. 4) even in the pure oxides, beyond the clear assignation of the high temperature peak (around 800 °C) which is proportional to the molar content of Ce. However, some conclusions could be derived: (1) corresponding peaks are generally located at lower temperatures in CP than SG samples, which denotes a higher degree of crystallinity, in agreement with XRD results; (2) crystalline phases are less defined in SG compared to CP samples, which produces a higher overlapping of the peaks; (3) the

Table 5 Results from H₂-TPR and NH₃-TPD of MnO_x-CeO₂ samples with different Mn and Ce content prepared by sol-gel and co-precipitation

Samples	Sol-gel		Co-precipitation			
	Mn oxidation state	Acidity ^a (μmol NH ₃ /g) (μmol NH ₃ /m ²)	Strong ac. weak ac.	Mn oxidation state	Acidity ^a (μmol NH ₃ /g) (μmol NH ₃ /m ²)	Strong ac. weak ac.
CeO ₂	--	129.1 (2.15)	1.1	--	204.1 (2.55)	1.1
15Mn85Ce	4.3	214.5 (3.20)	2.9	4.1	241.3 (2.87)	1.7
50Mn50Ce	3.9	200.7 (3.19)	1.6	3.5	304.5 (3.46)	2.0
85Mn15Ce	3.9	163.8 (2.87)	0.7	3.3	299.4 (3.44)	1.3
MnO _x	3.3	81.5 (5.43)	1.1	3.1	171.0 (5.03)	1.1

^a Acidity normalized to the surface area has been included in italics in brackets

^b Ratio. Weak acidity from 50 to 170 °C, and strong acidity from 170 to 450 °C

lowest temperature peaks (around 100 °C) are associated with reduction of surface species; (4) the two tiny peaks around 250–300 °C in the bimetallic samples prepared by CP are probably related to reduction of surface species; (5) the big wide peaks centered around 275 and 350 °C are mostly associated with the two reduction steps of Mn in the mixed oxide [44, 45].

The influence of Mn and Ce content on acid properties was studied by NH₃-TPD and by adsorption/desorption of pyridine followed by IR spectroscopy. Total acidity of the samples, summarized in Table 5, has been estimated from the integration of NH₃-TPD profiles. Mn and Ce interaction produces a significant improvement of acid properties, because total acidity of bimetallic samples is higher than that of pure cerium and manganese oxides. There is a maximum in total acidity corresponding to 15Mn85Ce composition in the sol-gel catalytic series and to 50Mn50Ce composition in the co-precipitation series. Moreover, it is important to note the overall higher acidity of co-precipitated samples with respect to the samples prepared by sol-gel. This fact, that has been already reported in the literature [35], is to be related mostly to the higher surface area provided by co-precipitation method. Thus, total acidity of the samples per unit surface area has been also included in Table 5 (in brackets).

The results show differences are much smaller, although the acidity of the co-precipitated 50Mn50Ce and, more clearly, 85Mn15Ce samples is still higher, which is probably related to the different crystal phases detected by XRD, together with the higher crystallinity (compared to the amorphous 85Mn15Ce SG sample).

Figure 5a and b show the NH₃ desorption profiles of the samples, together with obtained peak deconvolutions, which provide useful information about the effect of Mn and Ce content to the strength of acid sites. Although the general profiles of corresponding SG and CP samples are similar (except for the 85Mn15Ce), an additional intermediate peak was required to adequately fit the CP samples to Gaussian-type peaks. The desorption at low temperature is related to NH₃ adsorbed over weak acid sites, whereas the desorption at high temperature corresponds to the desorption of strongly adsorbed NH₃ [46, 47].

All samples, with little differences, present a common desorption peak around 100 °C, associated to weak acid sites. However, the main differences are associated to the intermediate-high temperature range. The presence of the mixed oxide in the bimetallic samples appears to increase the peak around 200 °C, whereas the decrease in crystallinity shifts the peak to lower temperatures and intensity.

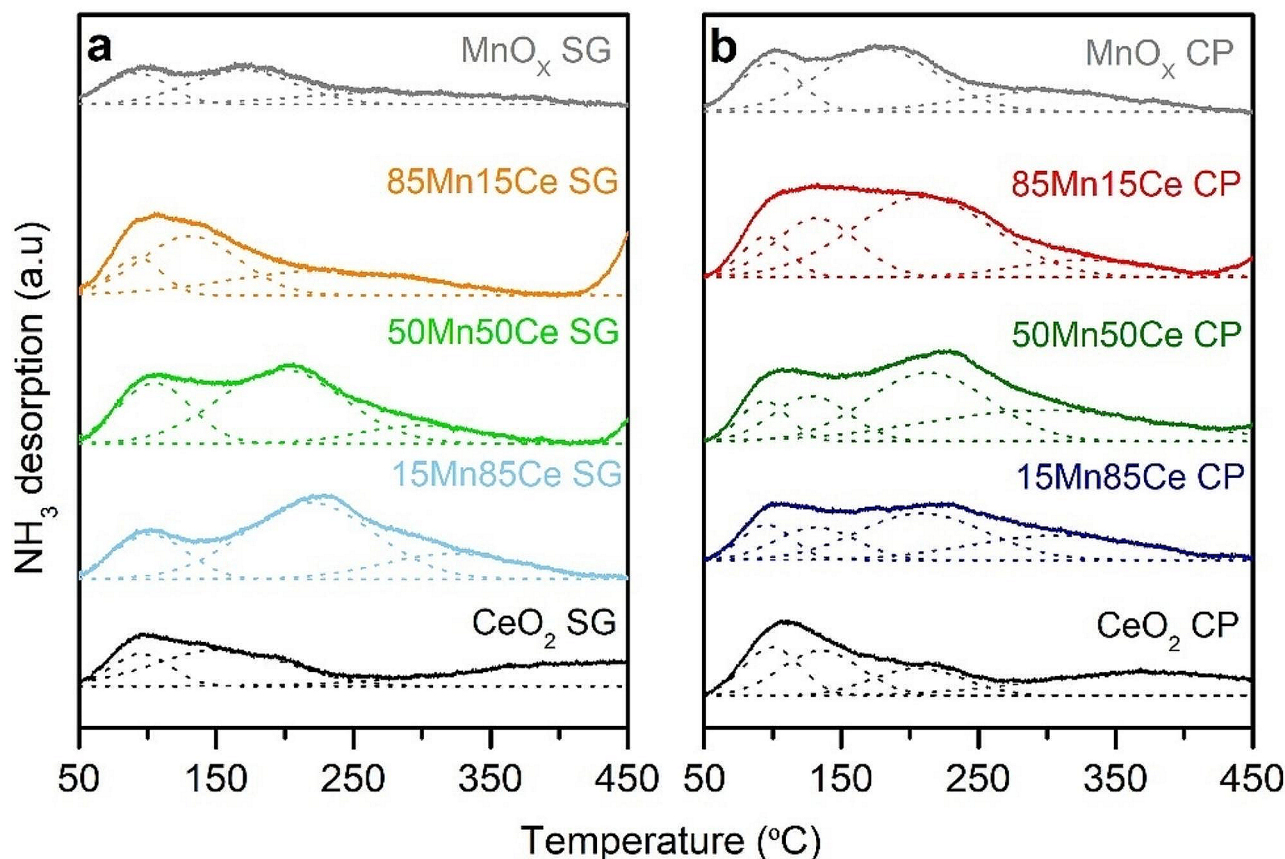


Fig. 5 NH₃-TPD profiles of MnO_x-CeO₂ samples with different Mn and Ce content prepared by (a) sol-gel and (b) co-precipitation

Table 5 also reports the ratio between strong and weak acidity. For the sake of simplicity, and to favor comparison between SG and CP samples, weak acidity was associated to NH_3 desorbed below 170°C , whereas NH_3 desorbed above this temperature was associated to strong acidity. The results indicate that the presence of non-amorphous mixed oxides leads to the formation of strong acid sites.

Moreover, the nature of acid sites was evaluated by the analysis of adsorbed pyridine. This analysis was carried out with the samples prepared by co-precipitation and the results are shown in Fig. 6. All sample spectra show bands around 1600 and 1572 cm^{-1} related to ν_{8a} vibrational mode, and also around 1482 and 1440 cm^{-1} that correspond to ν_{19b} vibrational mode of coordinated pyridine over Lewis acid sites [48, 49]. The strong noise between 1500 and 1400 cm^{-1} of the IR signal in the spectrum of the 85Mn15Ce sample is due to the presence of a strong band of carbonate species in the activated sample which leads to almost zero transmittance in this spectral region.

In the high wavenumber region, subtraction spectra of pure cerium oxide and 15Mn85Ce samples show a negative band at 3630 cm^{-1} . This band corresponds to the loss of characteristic hydroxyl group of cerium oxide because of the interaction with pyridine through H-bonds. In addition, a broad band at 3350 cm^{-1} , related to surface H-bonds, is noticeable in all catalysts but it is more intense in the Ce-rich samples. Although these results suggest the involvement of surface hydroxyl groups in the adsorption of pyridine, there is no evidence of bands associated to the formation of

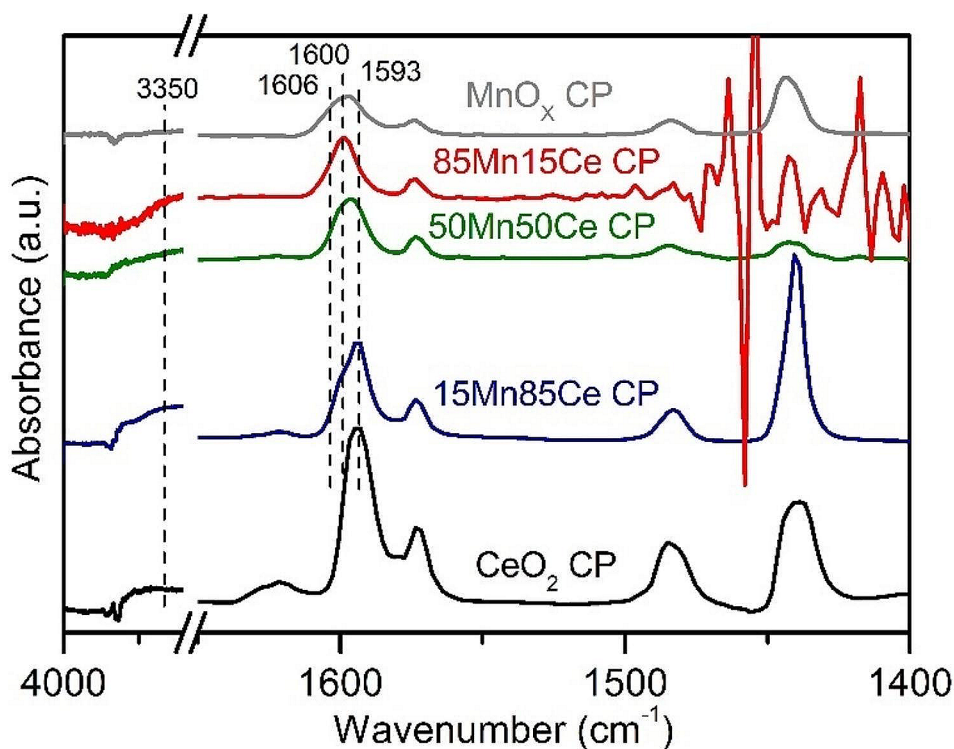
pyridinium ion over Brønsted acid sites; hence, these results conclude the studied samples only present Lewis acid sites together with weakly acidic OH groups.

The ν_{8a} vibrational mode of adsorbed pyridine shows some differences in position and shape depending on Mn content. Pure cerium oxide exhibits a well-defined band at 1593 cm^{-1} . Increasing Mn content leads to the formation of two shoulders around 1600 and 1606 cm^{-1} , the former becoming the main contribution in the 85Mn15Ce sample. The appearance of new contributions at higher wavenumber with Mn content denotes a different interaction between pyridine and surface acid sites depending on the composition of the catalysts, and the increase in Mn content favors the formation of more electron-withdrawing sites. The displacement of ν_{8a} vibrational mode to higher wavenumber is reported in the literature to be related to an increase in Lewis acid strength [50, 51], so, Mn ions behave as stronger Lewis acid sites, which is in agreement with that observed by NH_3 -TPD, where strong acid sites were promoted by Mn in high interaction with Ce.

In sum, Mn and Ce relative content has a significant effect on catalyst properties. At structural level, low Mn contents favor Mn incorporation to fluorite structure of cerium oxide leading to Mn species strongly interacting with Ce. On the other hand, the progressive increase in Mn content promotes a saturation of fluorite phase, which involves some segregation of Mn species.

Moreover, the segregation of Mn occurs differently depending on the preparation method, since sol-gel method

Fig. 6 FTIR subtraction spectra from pyridine adsorption and evacuation at room temperature of $\text{MnO}_x\text{-CeO}_2$ samples with different Mn and Ce content prepared by co-precipitation. The spectra of the corresponding activated surface have been subtracted



promotes an amorphous solid, whereas the phases that compose the samples prepared by co-precipitation exhibit a notable crystallinity degree. This fact also seems to affect the oxidation state of Mn species. Thus, Mn^{4+} species are promoted by sol-gel, whereas co-precipitation leads to the presence of Mn^{4+} and Mn^{3+} species, the former being more abundant at low Mn contents and the latter at high Mn contents.

The interaction degree between Mn and Ce is high, irrespective of the content of these metals, and this effect favors the formation of oxygen vacancies as a consequence of structural defects. Oxygen vacancies improve the reducibility of the samples compared to pure oxides. Similarly, metal content does not greatly affect the morphology and type of acid sites, mainly Lewis sites, although it has been corroborated that co-precipitation method leads to better morphological properties compared to sol-gel method, such as higher surface area and pore volume.

3.2 Catalytic Activity

After the analysis of the most important features of characterization, this section will assess the effect of Mn and Ce content on the simultaneous NO reduction and o-DCB oxidation. The objective here is not to deeply describe the reactions and their mechanisms, but to determine which of the prepared catalysts presents the best performance in the process. Figure 7 shows the NO and o-DCB conversion profiles of the samples. Pure cerium oxides hardly exhibit NO conversion below 200 °C. Above this temperature, NO conversion increases up to a maximum at 325 °C, above which the conversion drops. In the case of pure manganese oxides, markedly high NO conversion is obtained between 100 and 300 °C. This conversion curve shows an oscillatory profile that suggests the activation, as a function of temperature, of a set of multiple reactions that promote the consumption and formation of NO, and are related to the simultaneous conversion of o-DCB.

Bimetallic samples show different NO conversions depending on the Mn and Ce content, although there are no remarkable differences between those prepared by sol-gel and co-precipitation. The sample with the lowest Mn content, 15Mn85Ce, exhibits similar oscillatory trend to that of pure manganese oxide below 275 °C. In the case of the 50Mn50Ce and 85Mn15Ce samples, total NO conversion is obtained in the same temperature range. These results reveal that the most active catalysts are those with the highest Mn contents, which denotes Mn is the active metal. Nonetheless, the presence of Ce plays an important role, as there is a notable improvement in the catalytic activity of, for instance, the 85Mn15Ce samples with respect to

pure manganese oxides, despite the former having a lower Mn content.

At high temperatures, above 275 °C, NO conversion strongly drops in all bimetallic samples in a similar way as for pure oxides. This negative trend is observed for all catalysts, regardless of their composition, thus it is not caused by Mn and Ce content or preparation methods, but it is related to the activation of side-reactions leading to NO formation, such as NH_3 oxidation. In this sense, a similar drop in NO conversion at high temperature has been observed with other catalytic formulations, such as Fe-ZSM5 [52], VO_x/TiO_2 [53] and Pt/ Al_2O_3 [54]. In the following paragraphs, the assessment of the reaction by-products coming from NO reduction will provide more information about that.

It is important to remark that the temperature at which the drop in NO conversion occurs differs in each catalytic formulation. The more active the catalyst is, the lower is the temperature at which NO conversion starts to drop. In this sense, there is a remarkable difference between 85Mn15Ce and 50Mn50Ce samples (around 265 °C) and 15Mn85 samples (around 325 °C). This behavior agrees to the fact that side-reactions leading to NO formation become active at lower temperature with the most active catalysts.

As for o-DCB oxidation, Fig. 7c and d, conversion profiles for all samples show a particular S-shape composed by two steps. In each step, o-DCB conversion increases with temperature, and, between them, there is a small conversion drop. Total o-DCB conversion is achieved in the second step, located at high temperature, except for pure cerium oxide, which does not overcome the value of 80%. In bimetallic samples, the higher the Mn content, the higher the o-DCB conversion over the whole temperature range, both in the catalysts prepared by sol-gel and co-precipitation. This fact suggests an improvement of oxidative capability with Mn content. However, as in NO reduction, the presence of Ce also plays an important role in the catalytic activity because bimetallic samples with high Mn content (50Mn50Ce and 85Mn15Ce) lead to higher o-DCB conversion than pure manganese oxide, despite their lower Mn content.

The enhancement in oxidative capability in bimetallic samples is also observed in Table 6, as a decrease in T_{90} value (temperature at which o-DCB conversion reaches the value of 90%) with Mn content. This result shows that mixed oxide phase is not the only parameter that improves the catalytic activity in o-DCB oxidation, since the bimetallic catalysts with the highest Mn content (85Mn15Ce) exhibit the lowest values of T_{90} , even though their structural analysis showed that mixed oxide phase is not the main phase. In fact, the structural analysis showed a large contribution at structural level of segregated manganese oxide either with an amorphous structure, in the sample prepared

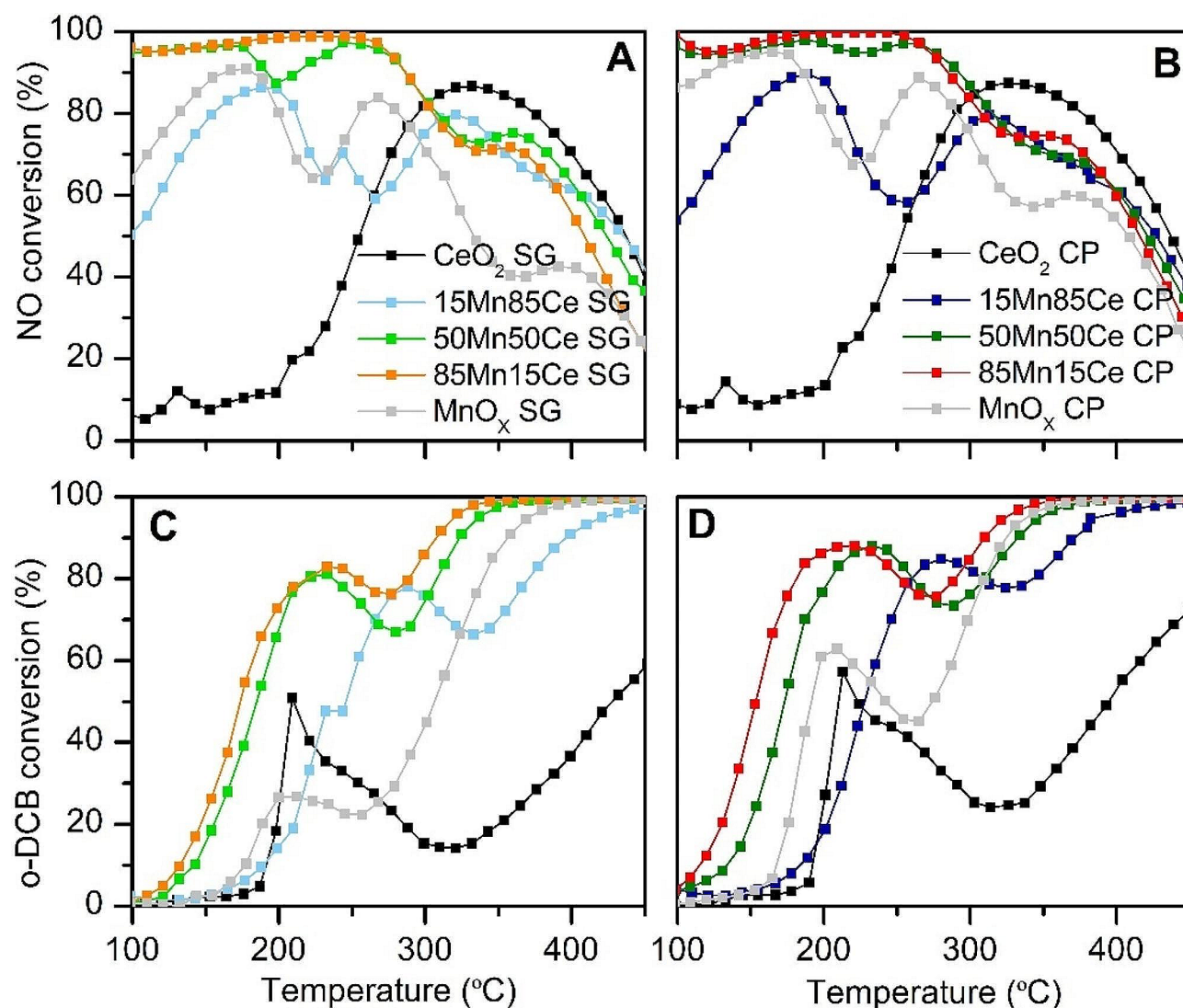


Fig. 7 NO conversion of $\text{MnO}_x\text{-CeO}_2$ samples with different Mn and Ce content prepared by (a) sol-gel and (b) co-precipitation. o-DCB conversion of the same samples prepared by (c) sol-gel and (d) co-precipitation.

Reaction conditions: feed stream: 300 ppm NO, 300 ppm NH_3 , 10% O_2 , 100 ppm o-DCB, and Ar to balance; GHSV: $40,000 \text{ h}^{-1}$; pressure: 1520 kPa

Table 6 T_{90} in o-DCB oxidation of $\text{MnO}_x\text{-CeO}_2$ samples with different Mn and Ce content. Reaction conditions: feed stream: 300 ppm NO, 300 ppm NH_3 , 10% O_2 , 100 ppm o-DCB, and Ar to balance; GHSV: $40,000 \text{ h}^{-1}$; pressure: 1520 kPa

Sample	T_{90} (°C)	
	Sol-gel	Co-precipitation
CeO_2	--	--
15Mn85Ce	400	375
50Mn50Ce	325	330
85Mn15Ce	320	310
MnO_x	340	325

with sol-gel, or as Mn_2O_3 phase, in the sample prepared by co-precipitation.

On this basis, the synergistic effect between mixed oxide phase and segregate manganese oxide, which leads to the

formation of different Mn species in high oxidation state, is proposed to be what promotes the best catalytic activity in the bimetallic catalysts with high Mn content.

On the other hand, when the results of o-DCB conversion are compared for each preparation method, the samples prepared by co-precipitation produce higher conversions than those prepared by sol-gel, especially at low temperature, coinciding with the first conversion step. This fact could be related to the higher surface area and total acidity provided by co-precipitation, as well as the synergy between mixed oxide phase and segregated Mn_2O_3 in the case of the bimetallic sample with the highest Mn content.

Therefore, the results above discussed have shown that bimetallic catalysts with the highest Mn content, 85Mn15Ce, are those with the best catalytic performance, although the

85Mn15Ce CP allows to obtain higher conversion in the oxidation reaction. Since this work studies the simultaneous removal of NO and o-DCB, a good catalytic performance involves obtaining high conversion of both compounds in the same temperature range. In this sense, the 85Mn15Ce CP catalyst leads to NO and o-DCB conversions above 80% in the temperature range between 180 and 250 °C. These results are significantly better than those obtained with V-based formulations and Mn-based catalysts in our previous studies [55].

The excellent catalytic properties of the 85Mn15Ce CP sample are related to the co-existence of a mixed oxide phase (with fluorite structure highly modified by the incorporation of Mn) and a segregated Mn_2O_3 phase. Each phase leads to the presence of different Mn species, whose oxidation state depends on the segregation degree of this metal. The variability of oxidation states allows to improve redox properties and also acidity. Moreover, structural defects caused by the interaction of both phases generate oxygen vacancies, which improves oxygen mobility and, consequently, the catalytic activity in oxidation reaction. Finally, the presence of both phases also leads to improving morphological properties, as higher surface area and pore volume were measured.

3.3 Catalytic Selectivity

The main by-products in NO reduction are N_2O and NO_2 . Their productions are shown in Fig. 8. Regarding N_2O , Fig. 8a and b, its production with pure cerium oxides is very low, whereas pure manganese oxide produces a significant amount of N_2O over the whole temperature range, its production being maximum between 200 and 300 °C.

N_2O is formed over the whole temperature range with bimetallic samples. The production profiles do not show a clear trend; however, it seems that more than one reaction participates in the production of N_2O , whose reaction rates change with temperature. Such hypothesis agrees with the NO conversion drops observed in Fig. 7. The maximum production of N_2O is quite similar regardless Mn content and significantly higher than that observed on pure cerium oxides, even for the bimetallic samples with the lowest Mn content, 15Mn85Ce. These results evidence that Mn species are strongly related to the formation of this by-product. In this sense, there are some discrepancies in the literature about the role of Mn in the production of N_2O . Some authors propose that the highly reactive oxygen of well-ordered manganese oxide is key for the production of N_2O [21, 56], whereas other researchers relate the production of N_2O to the Mn content and the reaction temperature [57]. In this work, increasing Mn content in bimetallic catalysts (related to the higher crystallinity degree of segregated manganese oxide phase) caused no remarkable differences

in the production of N_2O . Nonetheless, the fact that N_2O production with pure manganese oxide is lower than with bimetallic samples denotes Mn and Ce interaction is also important due to the promotion of oxidative capability that this entails.

NO_2 production (Fig. 8c and d) takes mostly place above 300 °C and sharply increases with temperature for all samples. Unlike N_2O , this is the typical temperature-dependent production profile. In the bimetallic catalysts, the increase in Mn content shifts the production profiles of NO_2 to lower temperatures and increases the amount of NO_2 produced. Both facts are associated to improvement of oxidative capability with Mn content.

Based on the results from the analysis of the catalytic activity in NO reduction, a strong drop in NO conversion was found around 275–300 °C. This behavior was above proposed to be related to the appearance of SCR side reactions, which would consume NH_3 necessary to carry out SCR. The results obtained in the analysis of SCR by-products agrees with the strong drop in NO conversion above mentioned, since an important production of both N_2O and NO_2 was found around 300 °C.

As for o-DCB oxidation, o-DCB is mostly completely oxidized to CO_2 and H_2O , and majority chlorine leaves the reactor as HCl. However, some o-DCB undergoes partial oxidation, producing CO and chlorinated organic compounds (identified as trichlorobenzene, tetrachloromethane and tetrachloroethylene) as the main by-products detected. The selectivity towards partial oxidation by-products is shown in Fig. 9 above 200 °C, i.e., when the o-DCB conversion is significant.

Figure 9a and b show that the CO selectivity of DCB conversion over pure cerium oxides increases progressively with temperature, not overcoming the value of 20% in the studied conditions. Bimetallic samples and pure manganese oxides exhibit similar profiles, in which CO selectivity slightly increases with temperature until reaching a plateau between 250 and 350 °C, temperature above which it strongly decreases. The maximum value of CO selectivity reached in the plateau at medium temperatures increases with Mn content in the catalysts prepared by both sol-gel and co-precipitation. This result denotes a small negative effect of Mn content over o-DCB total oxidation, despite the clear positive effect of Mn content on the oxidative capability above discussed. These two facts, which seem to be opposite, are completely compatible, since the improvement in the oxidative capability can favor o-DCB conversion, but, at the same time, can have a slightly negative effect on the total oxidation of o-DCB.

As for chlorinated organic compounds, Fig. 9c and d show that pure cerium oxides have a higher production of these compounds than pure manganese oxides. For

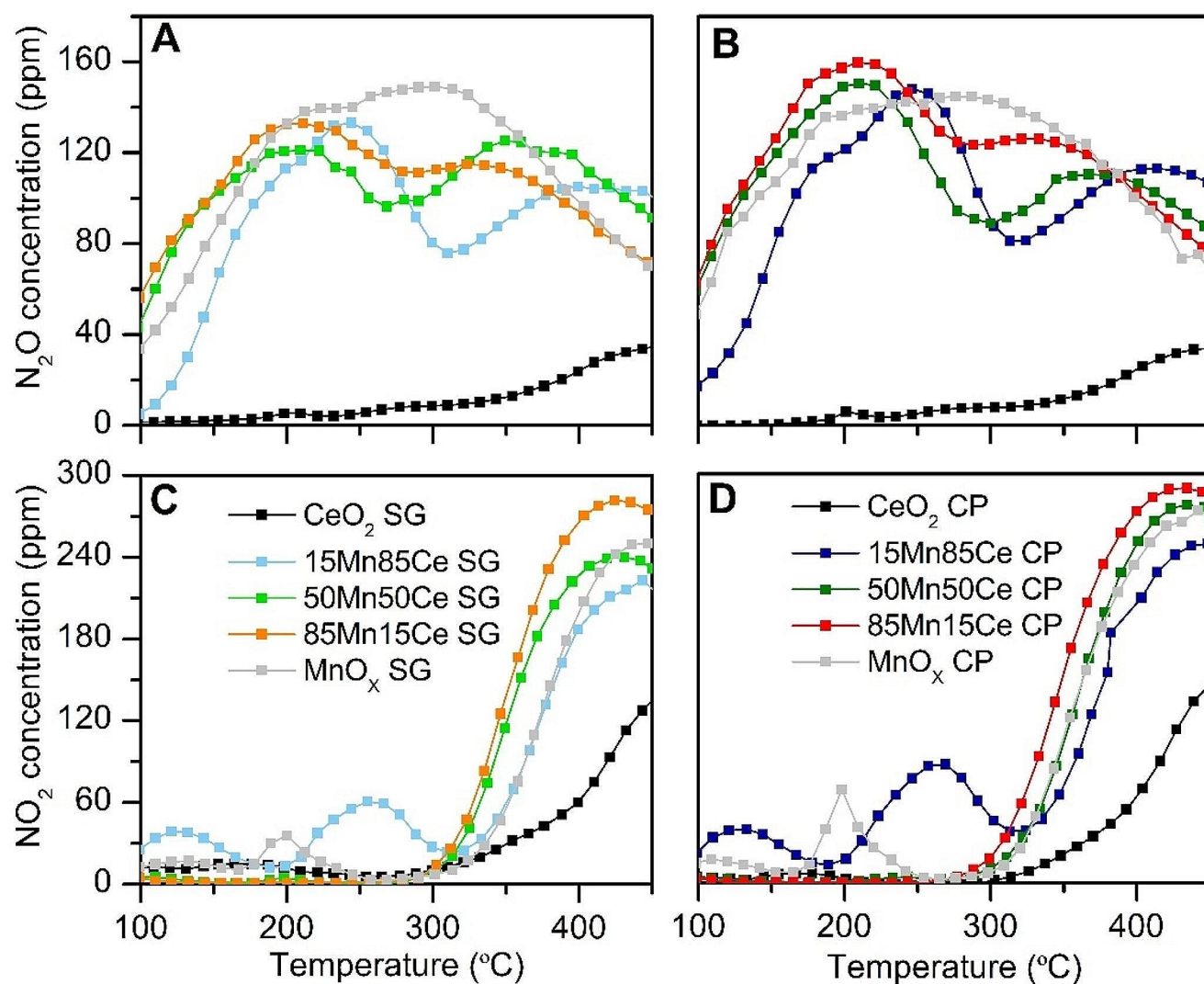


Fig. 8 N_2O production of $\text{MnO}_x\text{-CeO}_2$ samples with different Mn and Ce content prepared by (a) sol-gel and (b) co-precipitation. NO_2 production of the same samples prepared by (c) sol-gel and (d) co-pre-

cipitation. Reaction conditions: feed stream: 300 ppm NO, 300 ppm NH_3 , 10% O_2 , 100 ppm o-DCB, and Ar to balance; GHSV: $40,000 \text{ h}^{-1}$; pressure: 1520 kPa

bimetallic samples, the increase in Mn content leads to a decrease in the selectivity towards chlorinated organic compounds, in contrast to that observed for CO selectivity. This fact denotes that the improvement in oxidative capability promoted by Mn content also favors the oxidation of the chlorinated organic compounds involved in the different oxidation steps that compose the oxidation reaction pathway of o-DCB.

Therefore, the results discussed above point out that Mn and Ce content plays an important role in by-products production. This role is associated to the improvement in the oxidative capability promoted by the interaction between Mn and Ce and also by the presence of different crystalline phases at high Mn contents, as a consequence of Mn segregation. Thus, in NO reduction, the increase in Mn content

leads to increased N_2O and NO_2 production. In the case of oxidation reaction, the enhancement of oxidative capability decreases the selectivity towards chlorinated organic compounds, although it slightly increases that towards CO.

4 Conclusions

In this work, the effect of Mn and Ce content on $\text{MnO}_x\text{-CeO}_2$ catalytic formulation for carrying out simultaneous NO reduction and o-DCB oxidation has been analyzed, with the objective to choose the best performing catalyst. Mn and Ce content has a crucial role on the catalytic properties. At low Mn contents, Mn is incorporated into cerium oxide structure leading to a mixed oxide phase, which promotes

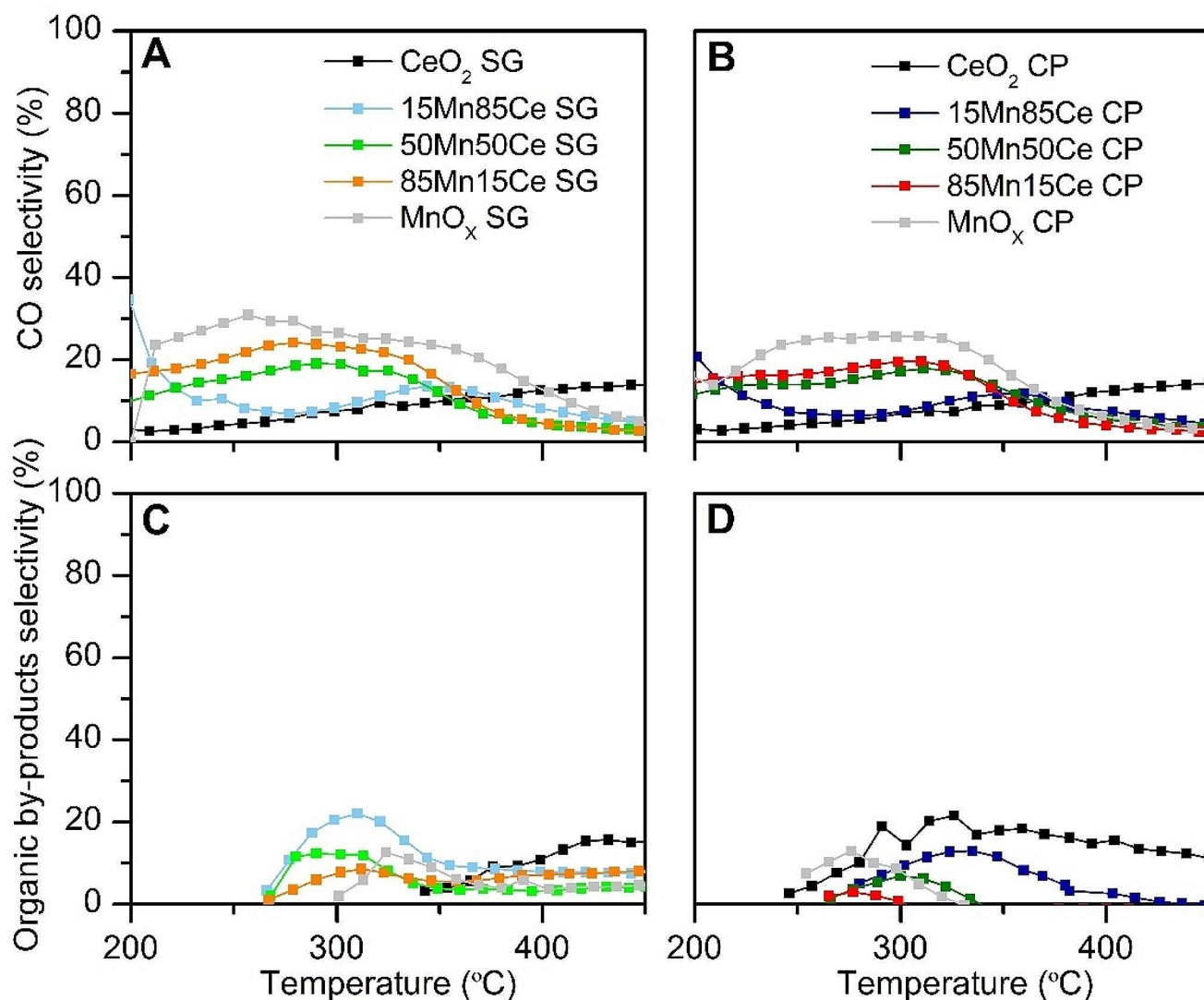


Fig. 9 CO selectivity of $\text{MnO}_x\text{-CeO}_2$ samples with different Mn and Ce content prepared by (a) sol-gel and (b) co-precipitation. Chlorinated organic compounds selectivity of the same samples prepared by

(c) sol-gel and (d) co-precipitation. Reaction conditions: feed stream: 300 ppm NO, 300 ppm NH_3 , 10% O_2 , 100 ppm o-DCB, and Ar to balance; GHSV: 40,000 h^{-1} ; pressure: 1520 kPa

Mn species in high interaction with Ce. The further increase in Mn content favors its segregation as a manganese oxide. This segregated manganese oxide phase coexists with the mixed oxide phase. Thus, at high Mn contents, two Mn species are detected: Mn in high interaction with Ce and segregated Mn.

The increase in Mn content allows to reach total NO conversion below 275 °C and shifts the o-DCB conversion profile to lower temperatures. Thus, the bimetallic catalysts with the highest Mn contents, 85Mn15Ce, exhibit the highest conversion levels of both NO and o-DCB, likely due to the coexistence of Mn in high interaction with Ce and segregated Mn. Comparing 85Mn15Ce SG and CP samples, the one prepared by co-precipitation has the best catalytic performance due to higher catalytic activity in oxidation

reaction. As a consequence, it has the widest activity temperature range: 180–250 °C, with NO and o-DCB conversions above 80% in the studied conditions.

The better catalytic activity of the 85Mn15Ce CP sample is related to the fact that this preparation method favors, on the one hand, better morphological properties (higher surface area and pore volume), and, on the other hand, the segregation of manganese oxide phase as Mn_2O_3 . The promotion of this segregated Mn_2O_3 together with the mixed oxide phase favors the presence of Mn species with different oxidation states (Mn^{4+} or Mn^{3+}). The synergy between the variability in Mn oxidation state and the oxygen vacancies, promoted by structural defects, is proposed to enhance redox properties. An increased in number and strength of acidic sites, mainly Lewis sites due to exposed Mn ions, can

also have an effect on catalytic activity. For instance, the coordination of o-DCB on acidic sites at the catalyst surface could make this electron-rich molecule more prone to the oxidation step. Mn and Ce content also affects by-product formation. Thus, in NO reduction, the presence of Mn leads to the production of N₂O and NO₂, although the increase in the content of this metal affects NO₂ production to a greater extent. This fact is associated to the enhancement in the oxidative capability promoted by the increase in Mn content. In oxidation reaction, the improvement of the oxidative capability decreases the selectivity towards chlorinated organic compounds, although it slightly increases that of CO.

Acknowledgements Authors acknowledge the financial support of Spanish Ministry for Science and Innovation (Project PID2019-107503RB-I00 by MCIN/AEI/<https://doi.org/10.13039/501100011033>) and Basque Government (Project IT1509-2022). JAMM specially thanks Spanish Ministry for Economy and Competitiveness and European Union (MINECO/ERDF, BES-2016-077849) for the PhD grant. The authors also acknowledge technical and human support provided by SGIker (UPV/EHU Advanced Research Facilities/ERDF, EU). Prof. G. Busca (Dipartimento di Ingegneria Civile, Chimica e Ambientale, Università di Genova, Italy) is gratefully acknowledged for the helpful discussion.

Funding Open Access funding provided thanks to the CRUE-CSIC agreement with Springer Nature.

Declarations

Competing Interests The authors have no competing interests to declare that are relevant to the content of this article.

Open Access This article is licensed under a Creative Commons Attribution 4.0 International License, which permits use, sharing, adaptation, distribution and reproduction in any medium or format, as long as you give appropriate credit to the original author(s) and the source, provide a link to the Creative Commons licence, and indicate if changes were made. The images or other third party material in this article are included in the article's Creative Commons licence, unless indicated otherwise in a credit line to the material. If material is not included in the article's Creative Commons licence and your intended use is not permitted by statutory regulation or exceeds the permitted use, you will need to obtain permission directly from the copyright holder. To view a copy of this licence, visit <http://creativecommons.org/licenses/by/4.0/>.

Reference

- Directive 2008/98/EC of the European Parliament and of the Council of 19 November 2008 on waste and repealing certain directives (Waste Framework Directive), Official Journal of the European Union L312 (22.11.2008) 3–30. <http://data.europa.eu/eli/dir/2008/98/2018-07-05>
- Cucchiella F, D'Adamo I, Gastaldi M (2017) *Energ Convers Manage* 131:18–31. <https://doi.org/10.1016/j.enconman.2016.11.012>
- Brunner PH, Rechberger H (2015) *Waste Manage* 37:3–12. <https://doi.org/10.1016/j.wasman.2014.02.003>
- Lai J, Wachs IE (2018) *ACS Catal* 8:6537–6551. <https://doi.org/10.1021/acscatal.8b01357>
- Busca G, Liotti L, Ramis G, Berti F (1998) *Appl Catal B-Environ* 18:1–36. [https://doi.org/10.1016/S0926-3373\(98\)00040-X](https://doi.org/10.1016/S0926-3373(98)00040-X)
- Finocchio E, Busca G, Notaro M (2006) *Appl Catal B-Environ* 62:12–20. <https://doi.org/10.1016/j.apcatb.2005.06.010>
- Du C, Lu S, Wang Q, Buekens AG, Ni M, Debecker DP (2018) *Chem Eng J* 334:519–544. <https://doi.org/10.1016/j.cej.2017.09.018>
- Sam-Cwan K, Hwan JS, Il-Rok J, Ki-Hun K, Myung-Hee K, Jae-Hyung K, Jun-Heung Y, Seung-Jin K, Jae-Cheon Y, Dong-Hee J (2001) *Chemosphere* 43:773–776. [https://doi.org/10.1016/S0045-6535\(00\)00432-X](https://doi.org/10.1016/S0045-6535(00)00432-X)
- Goemans M, Clarysse P, Joannès J, De Clercq P, Lenaerts S, Matthys K, Boels K (2004) *Chemosphere* 54:1357–1365. [https://doi.org/10.1016/S0045-6535\(03\)00255-8](https://doi.org/10.1016/S0045-6535(03)00255-8)
- European Commission JR, Centre, Neuwahl F, Cusano G, Gómez Benavides J, Holbrook S, Roudier S (2019) Best Available Techniques (BAT) reference document for waste incineration: Industrial Emissions Directive 2010/75/EU (Integrated Pollution Prevention and Control), Publications Office. <https://doi.org/10.2760/761437>
- Zhang S, Zhang B, Liu B, Sun S (2017) *RSC Adv* 7:26226–26242. <https://doi.org/10.1039/c7ra03387g>
- Jin R, Liu Y, Wu Z, Wang H, Gu T (2010) *Chemosphere* 78:1160–1166. <https://doi.org/10.1016/j.chemosphere.2009.11.049>
- Wang X, Zhang L, Wu S, Zou W, Yu S, Shao Y, Dong L (2016) *Catalysts* 6:112. <https://doi.org/10.3390/catal6080112>
- Li J, Chang H, Ma L, Hao J, Yang RT (2011) *Catal Today* 175:147–156. <https://doi.org/10.1016/j.cattod.2011.03.034>
- Wan Y, Zhao W, Tang Y, Li L, Wang H, Cui Y, Gu J, Li Y, Shi J (2014) *Appl Catal B-Environ* 148–149:114–122. <https://doi.org/10.1016/j.apcatb.2013.10.049>
- Kapteijn F, Singoredjo L, Andreini A, Moulijn JA (1994) *Appl Catal B-Environ* 3:173–189. [https://doi.org/10.1016/0926-3373\(93\)E0034-9](https://doi.org/10.1016/0926-3373(93)E0034-9)
- Tang X, Li J, Sun L, Hao J (2010) *Appl Catal B-Environ* 99:156–162. <https://doi.org/10.1016/j.apcatb.2010.06.012>
- Tang X, Hao J, Xu W, Li J (2007) *Catal Commun* 8:329–334. <https://doi.org/10.1016/j.catcom.2006.06.025>
- Kang M, Yeon TH, Park ED, Yie JE, Kim JM (2006) *Catal Lett* 106:77–80. <https://doi.org/10.1007/s10562-005-9194-3>
- Yang S, Wang C, Li J, Yan N, Ma L, Chang H (2011) *Appl Catal B-Environ* 110:71–80. <https://doi.org/10.1016/j.apcatb.2011.08.027>
- Kang M, Park ED, Kim JM, Yie JE (2006) *Catal Today* 111:236–241. <https://doi.org/10.1016/j.cattod.2005.10.032>
- Shi Y, Tang X, Yi H, Gao F, Zhao S, Wang J, Yang K, Zhang R (2019) *Ind Eng Chem Res* 58:3606–3617. <https://doi.org/10.1021/acs.iecr.8b05223>
- Yang S, Liao Y, Xiong S, Qi F, Dang H, Xiao X, Li J (2014) *J Phys Chem C* 118:21500–21508. <https://doi.org/10.1021/jp5062489>
- Qi G, Yang RT (2003) *J Catal* 217:434–441. [https://doi.org/10.1016/S0021-9517\(03\)00081-2](https://doi.org/10.1016/S0021-9517(03)00081-2)
- Shen B, Zhang X, Ma H, Yao Y, Liu T (2013) *J Environ Sci* 25:791–800. [https://doi.org/10.1016/S1001-0742\(12\)60109-0](https://doi.org/10.1016/S1001-0742(12)60109-0)
- Liu Z, Yi Y, Zhang S, Zhu T, Zhu J, Wang J (2013) *Catal Today* 216:76–81. <https://doi.org/10.1016/j.cattod.2013.06.009>
- Delimaris D, Ioannides T (2008) *Appl Catal B-Environ* 84:303–312. <https://doi.org/10.1016/j.apcatb.2008.04.006>
- Picasso G, Gutiérrez M, Pina MP, Herguido J (2007) *Chem Eng J* 126:119–130. <https://doi.org/10.1016/j.cej.2006.09.005>
- Li H, Lu G, Dai Q, Wang Y, Guo Y, Guo Y (2011) *Appl Catal B-Environ* 102:475–483. <https://doi.org/10.1016/j.apcatb.2010.12.029>

30. Wang X, Ran L, Dai Y, Lu Y, Dai Q (2014) *J Colloid Interf Sci* 426:324–332. <https://doi.org/10.1016/j.jcis.2013.10.007>
31. Wu Y, Zhang Y, Liu M, Ma Z (2010) *Catal Today* 153:170–175. <https://doi.org/10.1016/j.cattod.2010.01.064>
32. Xingyi W, Qian K, Dao L (2009) *Appl Catal B-Environ* 86:166–175. <https://doi.org/10.1016/j.apcatb.2008.08.009>
33. Cui M, Li Y, Wang X, Wang J, Shen M (2013) *J Rare Earth* 31:572–576. [https://doi.org/10.1016/S1002-0721\(12\)60322-6](https://doi.org/10.1016/S1002-0721(12)60322-6)
34. Tang X, Li Y, Huang X, Xu Y, Zhu H, Wang J, Shen W (2006) *Appl Catal B-Environ* 62:265–273. <https://doi.org/10.1016/j.apcatb.2005.08.004>
35. Martín-Martín JA, González-Marcos MP, Aranzabal A, González-Velasco JR (2023) *J Environ Chem Eng* 11:110200. <https://doi.org/10.1016/j.jece.2023.110200>
36. Ramana S, Rao BG, Venkataswamy P, Rangaswamy A, Reddy BM (2016) *J Mol Catal A-Chem* 415:113–121. <https://doi.org/10.1016/j.molcata.2016.01.028>
37. Ye Q, Xu B (2006) *Acta Phys-Chim Sin* 22:345–349
38. Sánchez Escribano V, Fernández López E, Panizza M, Resini C, Gallardo Amores JM, Busca G (2003) *Solid State Sci* 5:1369–1376. <https://doi.org/10.1016/j.solidstatesciences.2003.07.001>
39. Ambat I, Srivastava V, Haapaniemi E, Sillanpää M (2019) *Renew Energ* 139:1428–1436. <https://doi.org/10.1016/j.renene.2019.03.042>
40. Philip JT, Koshy CP, Mathew MD (2019) *Mater Res Express* 6:1150e1. <https://doi.org/10.1088/2053-1591/ab4fd5>
41. Julien CM, Massot M, Poinsignon C (2004) *Spectrochim Acta A* 60:689–700. [https://doi.org/10.1016/S1386-1425\(03\)00279-8](https://doi.org/10.1016/S1386-1425(03)00279-8)
42. Stobbe ER, De Boer BA, Geus JW (1999) *Catal Today* 47:161–167. [https://doi.org/10.1016/S0920-5861\(98\)00296-X](https://doi.org/10.1016/S0920-5861(98)00296-X)
43. Chen H, Sayari A, Adnot A, Larachi F (2001) *Appl Catal B-Environ* 32:195–204. [https://doi.org/10.1016/S0926-3373\(01\)00136-9](https://doi.org/10.1016/S0926-3373(01)00136-9)
44. Shen Q, Zhang L, Sun N, Wang H, Zhong L, He C, Wei W, Sun Y (2017) *Chem Eng J* 322:46–55. <https://doi.org/10.1016/j.cej.2017.02.148>
45. Wu Z, Tang N, Xiao L, Liu Y, Wang H (2010) *J Colloid Interf Sci* 352:143–148. <https://doi.org/10.1016/j.jcis.2010.08.031>
46. Ren S, Yang J, Zhang T, Jiang L, Long H, Guo F, Kong M (2018) *Chem Eng Res Des* 133:1–10. <https://doi.org/10.1016/j.cherd.2018.02.041>
47. Yao X, Ma K, Zou W, He S, An J, Yang F, Dong L (2017) *Chin J Catal* 38:146–159. [https://doi.org/10.1016/S1872-2067\(16\)62572-X](https://doi.org/10.1016/S1872-2067(16)62572-X)
48. Saad F, Comparot JD, Brahmi R, Bensitel M, Pirault-Roy L (2017) *Appl Catal A-Gen* 544:1–9. <https://doi.org/10.1016/j.apcata.2017.06.038>
49. Reddy CR, Nagendrappa G, Prakash BSJ (2007) *Catal Commun* 8:241–246. <https://doi.org/10.1016/j.catcom.2006.06.023>
50. Prescott HA, Li Z, Kemnitz E, Trunschke A, Deutsch J, Lieske H, Auroux A (2005) *J Catal* 234:119–130. <https://doi.org/10.1016/j.jcat.2005.06.004>
51. Albonetti S, Blasioli S, Bonelli R, Mengou JE, Scire S, Trifirò F (2008) *Appl Catal A-Gen* 341:18–25. <https://doi.org/10.1016/j.apcata.2007.12.033>
52. Long RQ, Yang RT (1999) *J Am Chem Soc* 121:5595–5596. <https://doi.org/10.1021/ja9842262>
53. Gallastegi-Villa M, Aranzabal A, Boukha Z, González-Marcos JA, González-Velasco JR, Martínez-Huerta MV, Bañares MA (2015) *Catal Today* 254:2–11. <https://doi.org/10.1016/j.cattod.2015.02.029>
54. Baik JH, Yim SD, Nam I, Mok YS, Lee J, Cho BK, Oh SH (2004) *Top Catal* 30:37–42. <https://doi.org/10.1023/b:toa.0000029725.88068.97>
55. Gallastegi-Villa M, Aranzabal A, González-Marcos JA, González-Velasco JR (2016) *Appl Catal B-Environ* 184:238–245. <https://doi.org/10.1016/j.apcatb.2015.11.006>
56. Park TS, Jeong SK, Hong SH, Hong SC (2001) *Ind Eng Chem Res* 40:4491–4495. <https://doi.org/10.1021/ie010218>
57. Kang M, Park ED, Kim JM, Yie JE (2007) *Appl Catal A-Gen* 327:261–269. <https://doi.org/10.1016/j.apcata.2007.05.024>

Publisher's Note Springer Nature remains neutral with regard to jurisdictional claims in published maps and institutional affiliations.